

## Electronic Supporting Information (ESI)

### Geometry-asymmetric photodetectors from metal-semiconductor-metal van der Waals heterostructures

Xiao Fu,<sup>#,a,b,c</sup> Tangxin Li,<sup>#,b,c</sup> Qing Li,<sup>#,a,b,c</sup> Chunhui Hao,<sup>a,c</sup> Lei Zhang,<sup>d</sup> Dejun Fu,<sup>e</sup> Jinjin Wang,<sup>b,c</sup> Hangyu Xu,<sup>b,c</sup> Yue Gu,<sup>b,c</sup> Fang Zhong,<sup>a,b,c</sup> Ting He,<sup>a,b,c</sup> Kun Zhang,<sup>b,c,f</sup> Gennady N. Panin,<sup>\*,g</sup> Wei Lu,<sup>a,b,c</sup> Jinshui Miao<sup>\*,a,b,c</sup> and Weida Hu<sup>\*,a,b,c</sup>

<sup>#</sup>These authors contributed equally to this letter

*a. School of Physics and Optoelectronic Engineering, Hangzhou Institute for Advanced Study, University of Chinese Academy of Sciences, Hangzhou 310024, China.*

*b. State Key Laboratory of Infrared Physics, Shanghai Institute of Technical Physics, Chinese Academy of Sciences, Shanghai 200083, China.*

*c. University of Chinese Academy of Sciences, Beijing 100049, China.*

*d. Ministry of Education Key Laboratory for Green Preparation and Application of Functional Materials, Hubei Provincial Key Laboratory of Polymers, School of Materials Science and Engineering, Hubei University, Wuhan 430062, PR China.*

*e. Wuhan University Shenzhen Research Institute, 6 Yuexin 2nd Rd., Nanshan Hitech Zone, Shenzhen 518057, China.*

*f. School of Physical Science and Technology, ShanghaiTech University, Shanghai 201210, China.*

*g. Institute of Microelectronics Technology and High-Purity Materials Russian Academy of Sciences, Chernogolovka, Moscow 142432, Russia*

## Supporting Information Section A: Materials

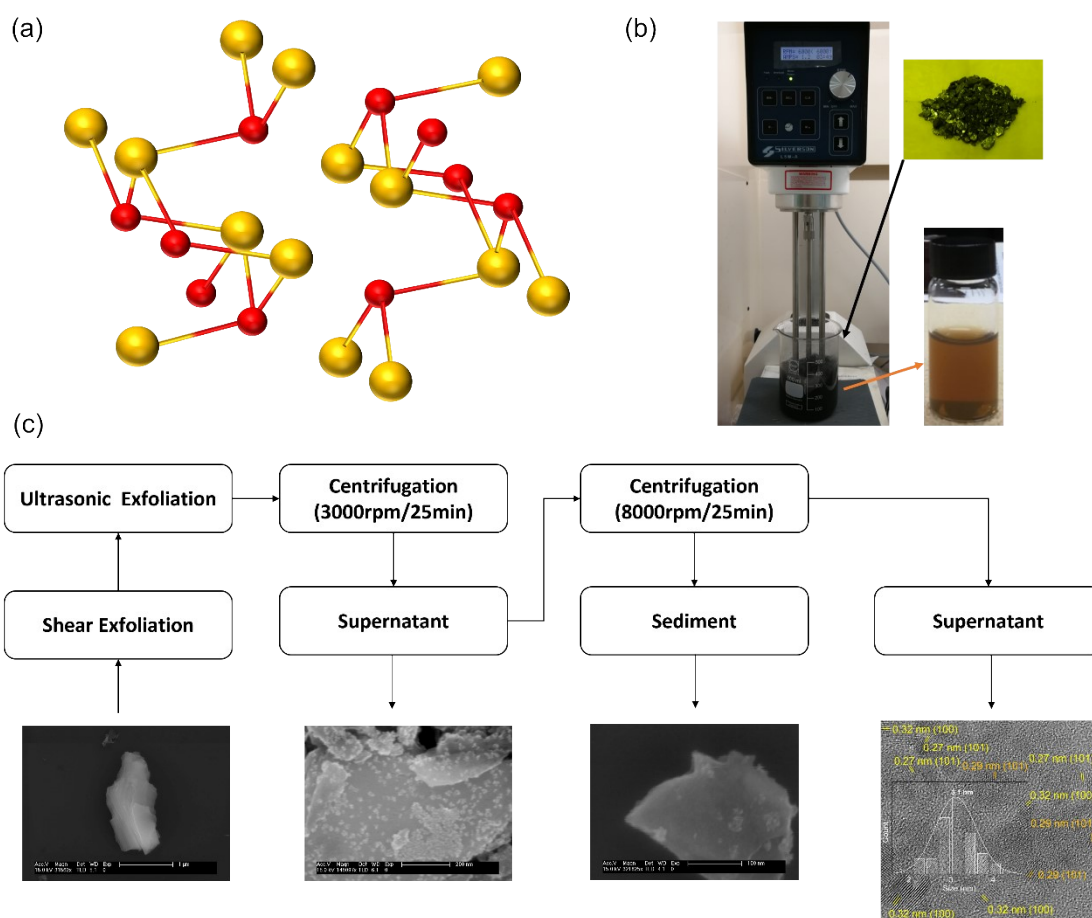


Fig. S1. (a) Schematic representation of SnS atoms in an orthorhombic lattice: Tin: yellow sphere; Sulphur: red sphere. (b) Photograph of an L5M high-shear mixer (Silverson Machines). (c) Schematic diagram of LPE and centrifugation processes for obtaining  $\text{Sn}_x\text{S}_y$  materials and the corresponding SEM and TEM images.

0.14 g of SnS granules (99.5%, Alfa Aesar) were dispersed and homogenized in 40 ml DI water and exfoliated using a L5M high-shear laboratory mixer (Silverson Machines) (Figure S6A and S6B).

*Preparation of NP-NS:* After shear mixing for 45 min at 5000 rpm, the dispersion is exposed in an intense ultrasonication by a horn-probe tip sonicator, operating at an amplitude of 28% and a pulse on / off for 9 sec and 1 sec, respectively, for 45 min,

using ice cooling to keep the temperature below 10°C. Then the dispersion is further treated by ultrasonic bath for 45 min with circulating water to keep the temperature below 13°C. Upon completion of the exfoliation step, the suspension is centrifuged for 25 min with 3000 rpm (Figure S6C). The collected supernatant is NP-NS.

*Preparation of NS and NP:* After preparing NP-NS, the dispersion is centrifuged for 25 min with 8500 rpm, then the top supernatant is collected as NP. The sediment is dissolved in 40 ml DI water with 1.5 min ultra-sonication. After repeating this process for 4 times, the dispersion dissolved in 40ml DI water is collected as NS.

Samples were examined using a Raman spectroscopy, SEM and HRTEM as shown in Fig. 1a and Fig. S1. Aqueous solutions of SnS particles,  $\text{Sn}_x\text{S}_y$  NP-NS, SnS NSs and NPs were deposited on sapphire substrates and measured using Raman spectroscopy. It is known that SnS has 21 optical phonons, of which 7 are infrared active modes ( $3B_{1u}$ ,  $1B_{2u}$  and  $3B_{3u}$ ), 2 are inactive ( $2A_u$ ), and the remaining 12 are Raman active modes ( $4A_g$ ,  $2B_{1g}$ ,  $4B_{2g}$  and  $2B_{3g}$ ) which can be measured from Raman spectra. However, it is known that SnS has strong anisotropic properties,<sup>1,2</sup> all phonon modes should be observed simultaneously only in randomly orientated SnS particles. Therefore, for atomic thin 2D layered crystals, the Raman spectrum changes dramatically compared to the Raman spectrum of SnS particles, as shown in the Fig. 1a.<sup>1</sup> The Raman spectrum of SnS powder has two broad bands of about  $169\text{ cm}^{-1}$  and  $212\text{ cm}^{-1}$ , and the weak peak at  $95\text{ cm}^{-1}$  is associated with the shift of the  $A_g$  mode of SnS.<sup>3</sup> Small peaks at about  $310\text{ cm}^{-1}$  indicate the presence of  $\text{SnS}_2$  phases.<sup>3</sup> Instead of broad bands of randomly oriented SnS particles, atomically thin SnS NS which separated from NP-NS show significant sharp peaks, which indicates the formation of high crystalline SnS NSs oriented in the [001] direction.<sup>1</sup> The peak at  $93\text{ cm}^{-1}$  belongs to the SnS  $A_g$  mode, which agrees well with various geometric scattering dependences.<sup>18 22</sup> The peaks at  $161\text{ cm}^{-1}$ ,  $185\text{ cm}^{-1}$  and  $215\text{ cm}^{-1}$  assigned to the  $B_{3g}$  and the two  $A_g$  modes of SnS, respectively.<sup>1,2,4</sup> These peaks indicate that SnS NSs exfoliated from the bulk crystal in the [001] direction abruptly changed

the optical modes. A very weak peak at about  $310\text{ cm}^{-1}$  refers to a very small number of  $\text{SnS}_2$  NPs remaining on the surface as shown in the SEM image of NS in Fig. 1a.

The Raman spectrum of NP shows peaks at  $160\text{ cm}^{-1}$  and  $182\text{ cm}^{-1}$  belonging  $B_{3g}$  and  $A_g$  modes of SnS, respectively, which have a slight redshift due to the confinement effect of the phonons.<sup>5,6</sup> A noticeable peak at about  $310\text{ cm}^{-1}$ , which is associated with  $\text{SnS}_2$ , indicates that mainly  $\text{SnS}_2$  NPs are formed. The size of the NPs is from 1 to 5 nm with an average size of 3.1 nm, according to the histogram (inset, Fig. S1C). Only small amount of the NPs have the lattice fringe spacing of 0.29 nm which coincides well with the (101) planes of the SnS lattice (Fig. S1C),<sup>7,8</sup> most of the NPs have 0.32 nm and 0.27 nm lattice fringes corresponding to the (100) and (101)  $\text{SnS}_2$  planes, respectively.<sup>9</sup> This indicates that mainly  $\text{SnS}_2$  NP and SnS NS were formed in this exfoliation process. The  $\text{Sn}_x\text{S}_y$  NP-NS sample shows a clear peak at  $310\text{ cm}^{-1}$ , indicating the presence of  $\text{SnS}_2$ , which is in good agreement with the  $\text{SnS}_2$  NPs observed in TEM. Instead of the sharp peaks observed in SnS NSs, broad bands with maxima at  $93.0\text{ cm}^{-1}$ ,  $161\text{ cm}^{-1}$  and  $215\text{ cm}^{-1}$  are observed due to NSs decoration by randomly oriented NPs.

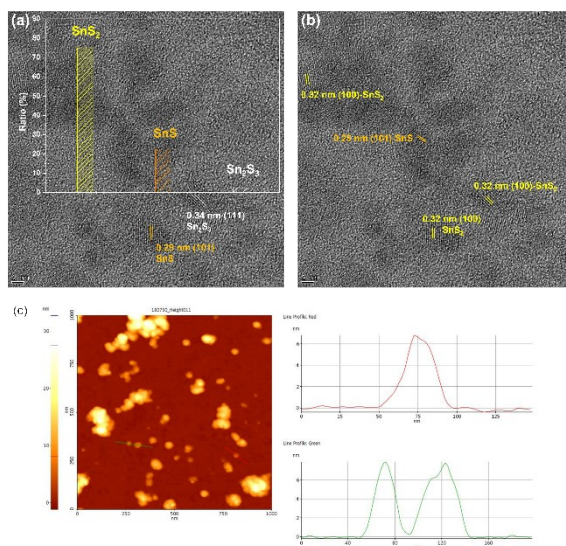


Fig. S2. (a, b) HRTEM image of  $\text{Sn}_x\text{S}_y$  NP. The inset in (a) shows the distribution diagram of the  $\text{SnS}_2$ ,  $\text{SnS}$  and  $\text{Sn}_2\text{S}_3$  NPs obtained by the LPE method. (c) AFM image of  $\text{SnS}$  NS.

Fig. S2 show the HRTEM image of  $\text{Sn}_x\text{S}_y$  NP,  $\text{SnS}$ ,  $\text{SnS}_2$  and  $\text{Sn}_2\text{S}_3$  NP can be found in the NP solution and more than 75% of the NP belong to  $\text{SnS}_2$ . Fig. S2c shows the AFM image of  $\text{SnS}$  NS, the thickness of  $\text{SnS}$  NS is about 6 nm.

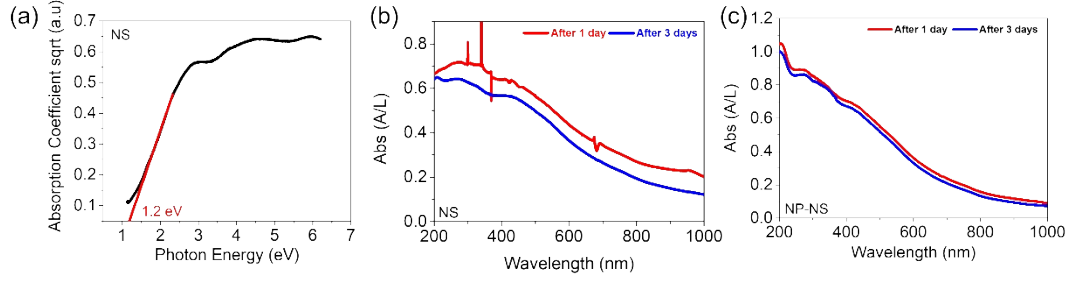


Fig. S3. (A) Plot of  $(\alpha hv)^{0.5}$  vs  $hv$  for various SnS NS, (B, C) UV-Vis absorption spectra of NS (B) and NP-NS (C) dispersions measured on the second and fourth days after preparation.

The optical properties of layered nanocrystals were investigated using UV-visible absorption spectroscopy. The spectra of  $\text{Sn}_x\text{S}_y$  nanocrystals were obtained over a broad wavelength range of 200-1000 nm (Fig. 2D). The relationship between the absorption coefficient  $\alpha$  and the photon energy is given by the following equation<sup>10</sup>:

$$(\alpha hv)^n = c(hv - E_g) \quad (S1)$$

where  $c$  is a constant with  $n = 2$  for direct and  $n = 0.5$  for indirect band gap transitions,  $\alpha$  is absorption coefficient, and  $E_g$  is the optical bandgap. The  $(\alpha hv)^{0.5}$  data are plotted against  $hv$  as shown in Fig. S3a and the inset of Fig. 2e. With decreasing size (increasing centrifugation speed), the absorption edge shifts to a shorter wavelength, and an optical bandgap of NS and NP is estimated to be 1.2 eV and 2.7 eV, respectively.

The increase in the energy gap can be explained by the strong quantum confinement effect in the  $\text{SnS}_2/\text{SnS}$  NPs. We estimated the Bohr radius of 2D  $\text{SnS}$  and  $\text{SnS}_2$  nanocrystals using the effective-mass approximation.<sup>11</sup>

the Bohr radius is:

$$r = \varepsilon(m_0/\mu)a_0 \quad (S2)$$

where  $\varepsilon$  is dielectric constant,  $a_0=0.053$  nm,  $m_0$  is the free-electron mass and  $\mu$  is the reduced mass of excitation given by:

$$\mu = m_e m_h / (m_e + m_h) \quad (S3)$$

For SnS, the effective masses of electron and hole are  $0.23m_0$  and  $0.25m_0$ , respectively.<sup>12</sup> The reduced masses of exciton of SnS and SnS<sub>2</sub> are  $0.12 m_0$  and  $0.3 m_0$ .<sup>10</sup> The dielectric constants of SnS and SnS<sub>2</sub> are 8 and 20.<sup>10,13</sup> Thus,  $r$  is calculated as 7 nm and 3.5 nm for SnS and SnS<sub>2</sub>, respectively. Hence SnS and SnS<sub>2</sub> will exhibit a quantum confinement effect with sizes less than 14 nm and 7 nm, respectively.

The dependence of the bandgap of NPs on the size was obtained in the effective-mass approximation.

$$E_{QD} = E_g + \frac{h^2}{8\mu r^2} - 1.8e^2/4\pi\epsilon\epsilon_0 r \quad (S4)$$

where  $h$  is the Plank constant and  $E_g$  is 1.1 eV.<sup>14</sup> The calculated result is shown in Fig. 2E.

Fig. S3b and c show the absorption spectra of NP-NS and NS, measured before and after three days storage. the slight changes in absorption spectra indicate good stability of NP-NS dispersions in pure water without a surfactant.

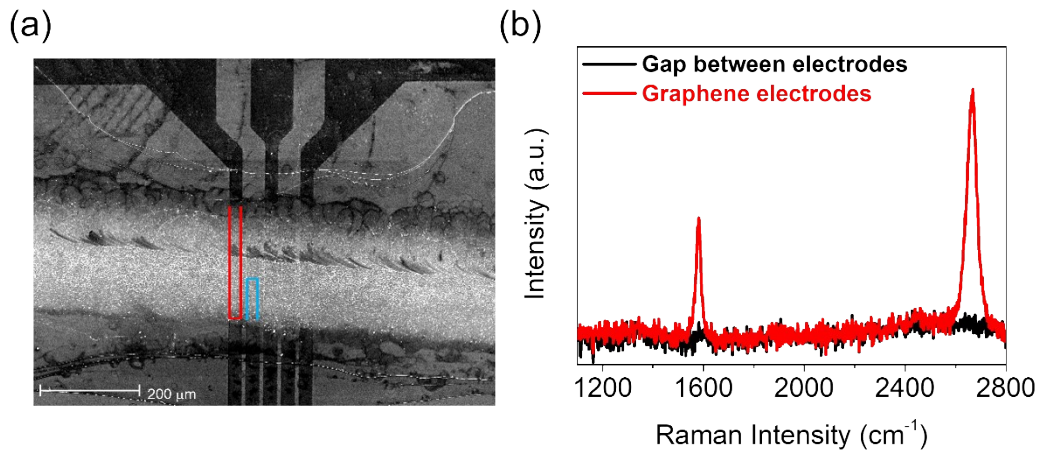


Fig. S4. (a) SEM image of NP-NS deposited on a  $\text{SiO}_2 / \text{Si}$  substrate with graphene electrodes. The red and blue areas show the contact regions between NP-NS and graphene. (b) Raman spectra of graphene electrodes.

The graphene layers were grown on the Cu foil by CVD method at  $1020^\circ\text{C}$  in methane/hydrogen flow at 600 mTorr, and then transferred onto  $\text{SiO}_2/\text{Si}$  substrates using PMMA. The graphene electrodes were prepared by photolithography and  $\text{O}_2$  plasma technique as shown in Fig. S4a. The graphene layer shows a weak peak D at  $1343 \text{ cm}^{-1}$  and peaks G and 2D located at  $1581 \text{ cm}^{-1}$  and  $2670 \text{ cm}^{-1}$ , respectively. It shows typical features of a high-quality graphene monolayer, such as the full width at half maximum (FWHM) for a 2D peak equal to  $44 \text{ cm}^{-1}$  and the  $I_{2D}/I_G$  and  $I_D/I_G$  ratios equal to 2.1 and 0.03, respectively. High quality single layer graphene is used as electrodes.

$\text{Sn}_x\text{S}_y$  film was formed on the Gr /  $\text{SiO}_2$  by spray deposition with a given shadow mask. Fig. S4a shows the SEM image of NP-NS deposited on a  $\text{SiO}_2 / \text{Si}$  substrate with graphene electrodes. The red and blue areas show the contact regions between NP-NS and graphene, the ratio of contact length can be controlled by moving the mask. (here the ratio is around 3.2).

## Supporting Information Section B: Modelling and Calculation

To systematic demonstrate the model proposed in our manuscript and describe the relationship degree of asymmetric geometry and rectification factor ( $I_{forward}/I_{reverse}$ ) in GA-MSM with limited contact ratio (usually less than 3). We established such model with standard Si as shown in Fig. S5-S8. Fig. S9 shows the rectification factor calculated from our model and the rectification factor calculated from Sentaurus Technology Computer Aided Design (TCAD) simulation with the same parameter. The rectification factor from TCAD simulation and Modeling calculation shows the similar variation tendency for various electron concentration, indicates the simplification of the calculation model is reasonable.

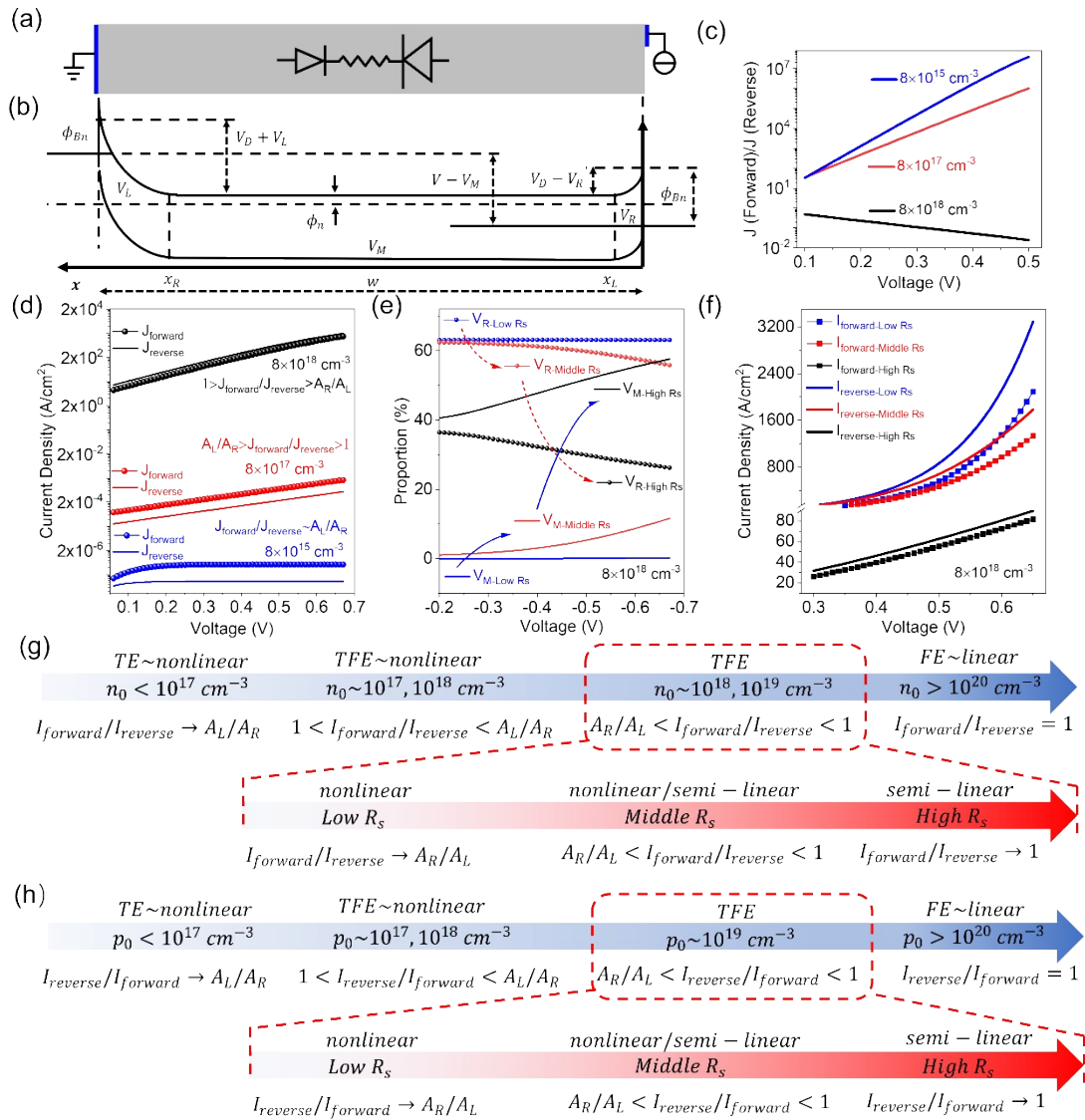


Fig. S5 (a) Schematic diagram of a GA-MSM. The inset shows the simplified device model of GA-MSM, the resistance of the left-side and right-side Schottky diodes are highlighted by the sizes of corresponding diode symbols. (b) The corresponding energy band diagram at forward bias voltage. (c) Plot of rectification factor ( $I_{forward}/I_{reverse}$ ) for a single junction at various electron concentration. (d) The current density of MSM device with asymmetric geometries for various electron concentration. (e) The voltage distribution of a GA-MSM at low (blue curve), middle (red curve) and high (black curve) channel resistance, the solid line represents the voltage distributed on channel, and the sphere represent the voltage distributed on right-side tunnelling diode. (f) Theoretical current-voltage characteristics for an GA-MSM at low (blue curve), middle (red curve) and high (black curve) channel resistance. (g, h) Representation of the theoretical rectification factor characteristics at various electron (g) / hole (h) concentration and the corresponding rectification factor at various channel resistance.

All calculations and TCAD simulation in Fig. S5-9 are based on the parameters of a standard Si, which record from TCAD manual. The tunneling effective mass is  $0.07 m_0$ .<sup>15,16</sup> The ratio of contact length is 5 (left/right) and by increase the width of channel, we can obtain the low ( $5 \mu m$ ), middle ( $500 \mu m$ ) and high ( $50000 \mu m$ )  $R_s$ .

Without loss of generality, we consider a GA-MSM structure with a n-type semiconductor as schematically shown in Fig. S5a. Here, we only consider a device with a limited ratio of asymmetric contact geometries working in a low voltage range, which indicates the hole current and electric field in Y direction is on the orders lower than that of electron current and the electric field in X direction (Fig. S6 and S7).<sup>17</sup> Thus, we simplify this MSM into two back-to-back Schottky diodes with a channel resistor ( $R_s$ ) as shown in the inset of Fig. S5a. The corresponding energy band diagram is shown in Fig. S5b, where  $\phi_{Bn}$  is the barrier height for metal and n-type semiconductor,  $\phi_n$  is the difference between

valance band and Femi level,  $w$  is the width of MSM structure,  $V_D$  is built-in potential for metal-semiconductor,  $V_R$ ,  $V_M$  and  $V_L$  are the voltage drop on right side junction, channel and left side junction when a forward voltage  $V$  is applied.

When the concentration of electron is on the order of  $10^{15} \text{ cm}^{-3}$ , the TE will dominate the current transport, for a device working in low voltage range, the barrier lowering effect can be negligible,<sup>17</sup> according to the theory of thermionic emission,<sup>18,19</sup> we have:

$$J_{TE,R} = A_n T^2 e^{-\frac{q\phi_{Bn}}{kT}} \left( e^{\frac{qV_R/n_{id}kT}} - 1 \right) \quad (S5)$$

$$J_{TE,L} = A_n T^2 e^{-\frac{q\phi_{Bn}}{kT}} \left( 1 - e^{-\frac{qV_L/n_{id}kT}} \right) \quad (S6)$$

where  $J_{TE,R}$  and  $J_{TE,L}$  is the current density go through right-side and left-side junction, respectively,  $k$  is the Boltzmann constant,  $T$  is the temperature,  $q$  is electric charge,  $n_{id}$  is ideality factor and  $A_n$  is the effective Richardson constant for electrons, while the current density go through channel ( $J_{TE,RS}$ ) should be:

$$J_{TE,RS} = q\mu_n n \frac{V_M}{w - w_L - w_R} \quad (S7)$$

where  $n$  is electron concentration,  $\mu_n$  is the electron mobility,  $w_L$  and  $w_R$  are the width of depletion width of left and right contact, respectively, which defined by:

$$w_L = \sqrt{\frac{2\varepsilon_r(V_D + V_L)}{qN}} \quad (S8)$$

$$w_R = \sqrt{\frac{2\varepsilon_r(V_D - V_R)}{qN}} \quad (S9)$$

where  $\varepsilon_r$  is the dielectric constant and  $N$  is the ionized impurity concentration.

From current continuity requirements we have:

$$V_R + V_M + V_L = V \quad (S10)$$

$$I_{TE,R} = I_{TE,Rs} = I_{TE,L} \quad (S11)$$

where  $I_{TE,R}$ ,  $I_{TE,Rs}$ ,  $I_{TE,L}$  are the current go through right-side junction, channel, and left-side junction, which defined by:

$$I_{TE,R} = A_R J_{TE,R} \quad (S12)$$

$$I_{TE,Rs} = \frac{(A_R + A_L)}{2} J_{TE,Rs} \quad (S13)$$

$$I_{TE,L} = A_L J_{TE,L} \quad (S14)$$

where  $A_R$  and  $A_L$  are the contact areas of right-side and left-side junctions, which should be equal to the thickness multiplied by corresponding contact length.

Similar calculation model can be established for TFE current transport:<sup>20</sup>

$$J_{TFE,R} = \frac{A^* T \sqrt{\pi E_{00} q (\phi_{Bn} - \phi_n - V_R)}}{k \cosh\left(\frac{E_{00}}{kT}\right)} e^{\left[\frac{-q\phi_n}{kT} - \frac{q(\phi_{Bn} - \phi_n)}{E_0}\right]} e^{qV_R/E_0} \quad (S15)$$

$$J_{TFE,Rs} = qn\mu_n \frac{V_M}{w} \quad (S16)$$

$$J_{TFE,L} = \frac{A^* T}{k} \sqrt{\pi E_{00} q \left( V_L + \frac{\phi_n}{\cosh^2\left(\frac{E_{00}}{kT}\right)} \right)} e^{\left(\frac{-q\phi_{Bn}}{E_0}\right)} e^{qV_L/\varepsilon'} \quad (S17)$$

where  $J_{TFE,R}$ ,  $J_{TFE,Rs}$  and  $J_{TFE,L}$  are the TFE current density go through right-side junction, channel, and left-side junction, respectively,  $A^*$  is the effective Richardson constant,  $E_{00}$ ,  $E_0$ ,  $\varepsilon'$  are defined by following equations:

$$E_{00} = \frac{qh}{4\pi} \sqrt{\frac{N}{m^* E_r}} \quad (S18)$$

$$E_0 = E_{00} \coth\left(\frac{E_{00}}{kT}\right) \quad (S19)$$

$$\varepsilon' = \frac{E_{00}}{\frac{E_{00}}{kT} - \tanh\left(\frac{E_{00}}{kT}\right)} \quad (S20)$$

where  $m^*$  is the tunneling effective mass. Thus, we have:

$$I_{TFE,R} = I_{TFE,Rs} = I_{TFE,L} \quad (S21)$$

where  $I_{TFE,R}$ ,  $I_{TFE,Rs}$ ,  $I_{TFE,L}$  are the TFE current go through right-side junction, channel, and left-side junction, which defined by:

$$I_{TFE,R} = A_R J_{TFE,R} \quad (S22)$$

$$I_{TFE,Rs} = \frac{(A_R + A_L)}{2} J_{TFE,Rs} \quad (S23)$$

$$I_{TFE,L} = A_L J_{TFE,L} \quad (S24)$$

Taking all parameters of a n-type semiconductor (using silicon material for simplicity), the calculated results of various electron concentrations and channel resistance ( $R_s$ ) are shown in Fig. S5c-f. Fig. S5c shows the rectification factor of a single metal-semiconductor contact for various electron concentrations. When the concentration is low, the reverse current is much lower than forward current (Fig. S5c, blue curve) due to TE current transport, indicates the resistance of reverse-biased diode is much higher than forward-biased diode. Thus, the voltage dropped on the left/right side diode ( $V_L/V_R$ ) should be almost equal to the total voltage ( $V$ ) when a forward/reverse bias voltage is applied on the GA-MSM structure, according to equation (8) and (10), the rectification factor is almost equal to the ratio of corresponding contact area/length ( $A_L/A_R$ ) as shown in Fig. S5d (blue curve).

When the electron concentration is on the order of  $10^{17} \sim 10^{18} \text{ cm}^{-3}$ , the value of  $E_{00}$  is smaller but comparable to  $kT$ , TFE will dominate the current transport, different from an ultrahigh value of TE dominated on/off ratio, the red curve in Fig. S5c shows a much lower on/off ratio when a forward/reverse bias voltage is applied on a single diode, indicates the voltage drops on forward biased diode is not negligible (Fig. S3),

resulting a smaller rectification factor compared to the ratio of corresponding contact area ( $A_L/A_R$ ) as shown in Fig. S5d (red curve).

When the electron concentration is on the order of  $10^{18}\sim 10^{19}$   $\text{cm}^{-3}$ , the value of  $E_{00}$  is bigger but comparable to  $kT$ . Fig. S5c (black curve) shows an on/off smaller than 1, on the other hand, the TFE current is increased by orders when the electron concentration is high enough, thus, the  $R_s$  is comparable with the resistance of the tunneling diodes, indicates a quite different voltage distribution of MSM structure. Fig. S5e shows the voltage distribution of various value of  $R_s$  when a reverse bias voltage is applied. When the  $R_s$  is quite low, the voltage will mainly drop on left-side tunneling diode as shown in Fig. S5e (blue curve), leading to a nonlinear and subexponentially increased I-V curve (Fig. S5f, blue curve) as the current is proportional to  $\sqrt{\pi E_{00} q (\phi_{Bn} - \phi_n - V_L)} e^{qV_L/E_0}$ . The rectification factor should be bigger and closer to the ratio of corresponding contact area/length ( $A_R/A_L$ ) which is smaller than 1 (Fig. S5f blue curve). When the value of  $R_s$  is increased, the voltage dropped on channel is not negligible and the proportion of voltage dropped on left-side tunneling diode will be decreasing as shown in Fig. S5e (red curve), leading to a rectification factor larger than corresponding contact area ( $A_R/A_L$ ) and closer to 1 (Fig. S5f, red curve). When the value of  $R_s$  is further increased, the voltage will mainly drop on channel as shown in Fig. S5e (black curve), indicates a semi-linear I-V curve and a rectification factor almost equal to 1 (Fig. S5f, black curve). For an ultra-high electron concentration more than  $10^{20}$   $\text{cm}^{-3}$ , FE will dominate the current transport, and voltage will drop on channel resistor, leading to a linear I-V curve without considering of the contact length.<sup>21</sup>

Similar simulation data from Sentaurus TCAD are shown in Fig. S8, which demonstrate same variation tendency, to this end, we summaries all calculation and analyses in Fig. S5g. When  $E_{00}$  is much lower than  $kT$ , TE will dominate the current transport and the rectification factor ( $I_{forward}/I_{reverse}$ ) of such a MSM is very close to

the ratio of corresponding contact area ( $A_L/A_R > 1$ ). When  $E_{00}$  is smaller but comparable than  $kT$ , TFE will dominate the current transport and the rectification factor ( $I_{forward}/I_{reverse}$ ) of such a MSM is smaller than the ratio of corresponding contact area ( $A_L/A_R > 1$ ) and bigger than 1. When  $E_{00}$  is bigger but comparable than  $kT$ , although the TFE still dominate the current transport, but the voltage dropped on tunneling diodes should be opposite to previews cases, the voltage distribution and I-V curve will strongly depend on the  $R_s$ . For a low  $R_s$ , the I-V curve is nonlinear and the rectification factor ( $I_{forward}/I_{reverse}$ ) should be closer and bigger than the ratio of corresponding contact area ( $A_R/A_L < 1$ ), we note that this ratio is inversely related to previews cases due to the opposite voltage distribution. When the  $R_s$  is increased, the rectification factor ( $I_{forward}/I_{reverse}$ ) is bigger than the ratio of corresponding contact area ( $A_R/A_L < 1$ ) and close to 1. For a high  $R_s$ , the semi-linear I-V curve will be obtained and the rectification factor ( $I_{forward}/I_{reverse}$ ) is closer to 1. We note that all analyses on a p-type semiconductor should be opposite as the direction of built-in electric field is opposite. Fig. S5h represent the dependence of inverse rectification factor ( $I_{reverse}/I_{forward}$ ) and ratio of contact areas (Fig. S8).

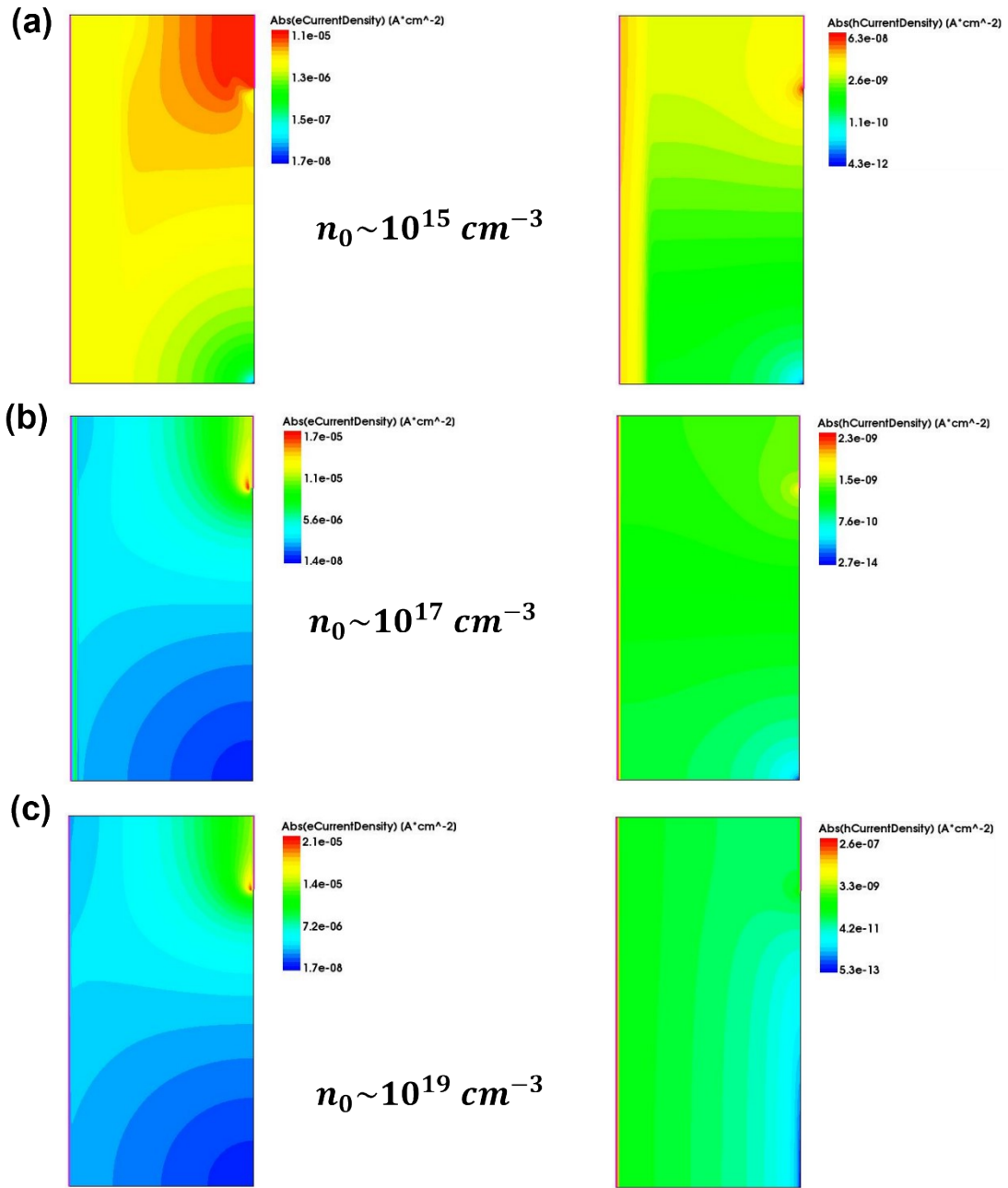


Fig. S6. The TCAD simulated electron (left) and hole (right) current density of a GA-MSM based on a n-type Si at a 1V bias voltage, the electron concentration are on the order of  $10^{15} \text{ cm}^{-3}$  (A),  $10^{17} \text{ cm}^{-3}$  (B) and  $10^{19} \text{ cm}^{-3}$  (C), the width of the structure is  $5 \mu\text{m}$ .

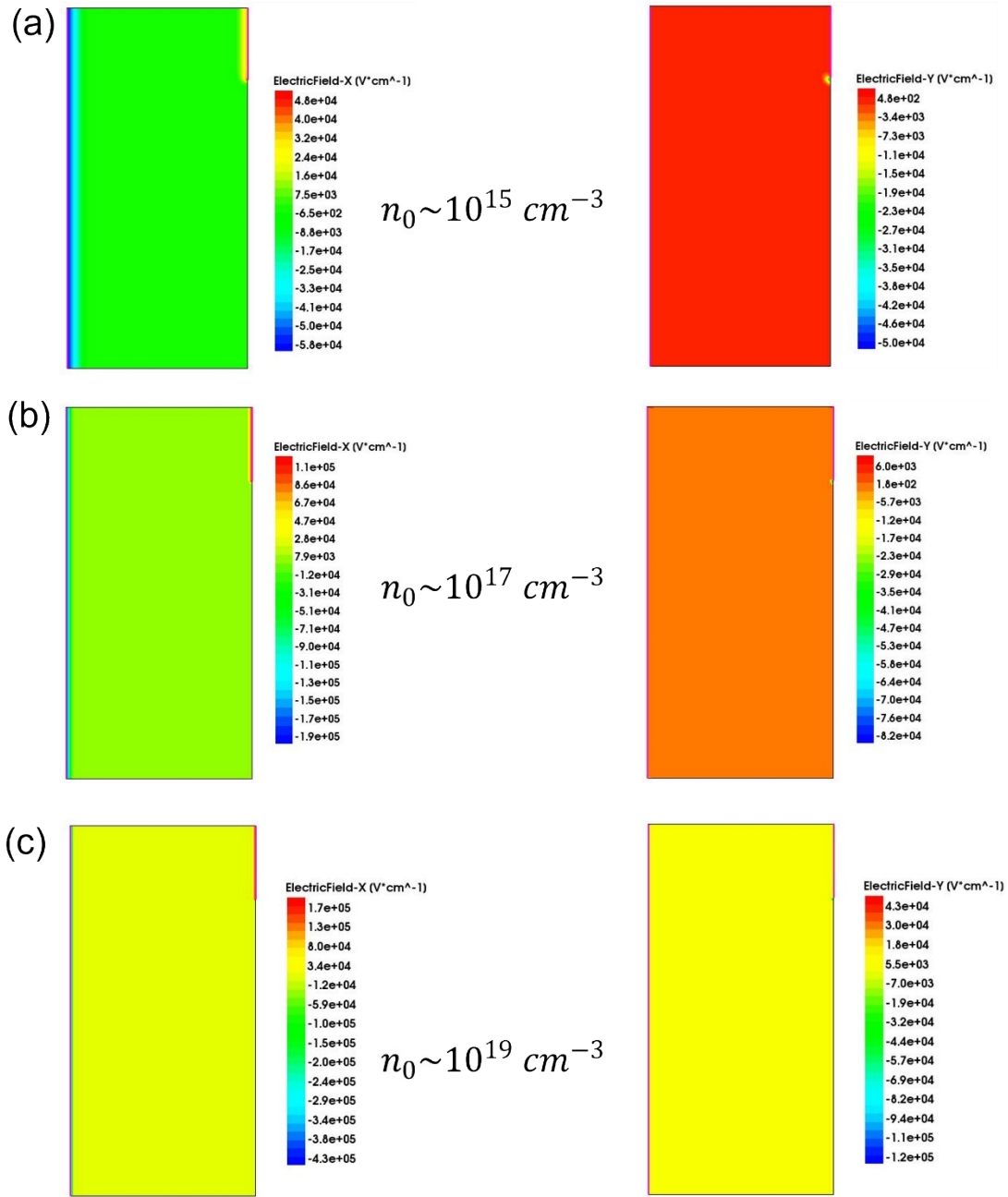


Fig. S7. The TCAD simulated electric field of X direction and Y direction of a GA-MSM based on a n-type Si at a 1V bias voltage, the electron concentration are on the order of  $10^{15} \text{ cm}^{-3}$  (A) ,  $10^{17} \text{ cm}^{-3}$  (B) and  $10^{19} \text{ cm}^{-3}$  (C), the width of the structure is  $5 \mu\text{m}$ .

Fig. S6 and S7 show the TCAD simulated electron (S6, left) and hole (S6, right) current density and electric field of X direction and Y direction of a GA-MSM based on

a n-type Si at a 1V bias voltage for various carrier concentration, the majority current density is apparently several orders higher than that of minority current density, and the electric field of X direction is about 1~2 orders higher than that of Y direction.

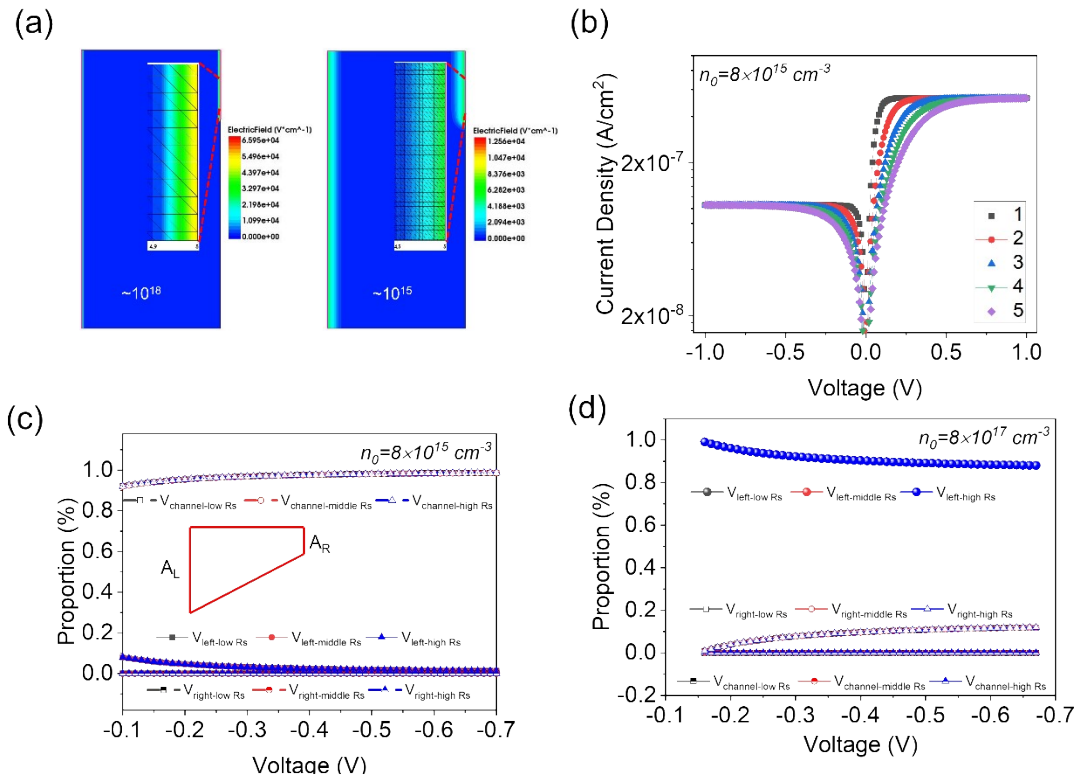


Fig. S8: (a) Stimulated electric field (absolute value) of Gr/SnS/Gr GA-MSM at low and high concentration. (b) The calculated I-V curve for a GA-MSM with n-type Si at various ideality factor. (c, d) The voltage distribution of a GA-MSM with n-type Si at various electron concentration.

Fig. S8a shows the stimulated electric field (absolute value) of Gr/SnS/Gr GA-MSM at low and high concentration, although the depletion region is a little different from symmetric contact geometries, however, those difference can be negligible when the sum of the width of depletion region is much lower than the length and width of the device. Fig. S8b shows the calculated I-V curve at various ideality factor based on our model. Fig. S8c and S8d show the calculated voltage distribution of a GA-MSM with n-

type Si at an electron concentration of  $8 \times 10^{17} \text{ cm}^{-3}$  and  $8 \times 10^{18} \text{ cm}^{-3}$  based on our model. When the sum of depletion width is much lower than the length and width of device, approximately, we assume the channel resistance is considered as the resistance of a trapezoid as shown in the inset of Fig. S8c, thus,  $R_s = \frac{A_L + A_R}{2} R_0$ . Due to the resistance of diode is much higher than that of channel resistance, the dependence of voltage distribution with channel resistance becomes largely irrelevant.

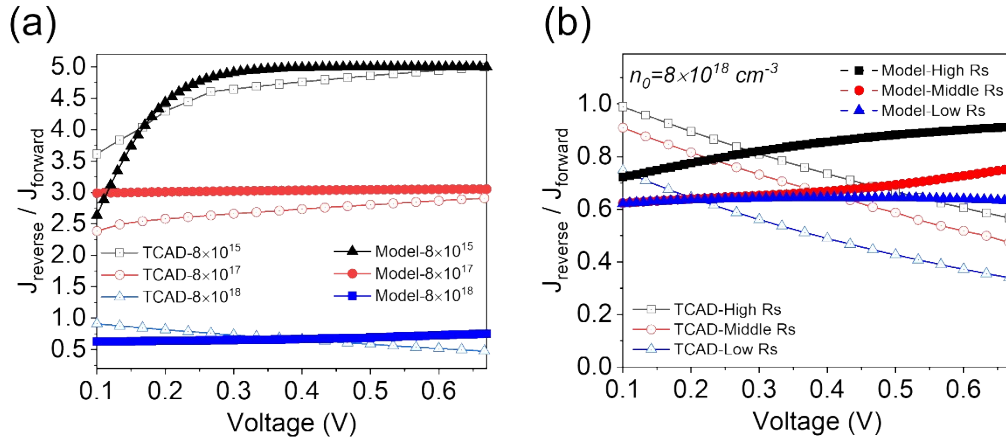


Fig. S9. The comparison of TCAD simulation results and Modeling calculation results for an GA-MSM based on n-type Si at various electron concentration (a) and channel resistance (b).

The rectification factor from TCAD simulation and Modeling calculation shows the similar variation tendency for various electron concentration, indicates the simplification of the calculation model is reasonable.

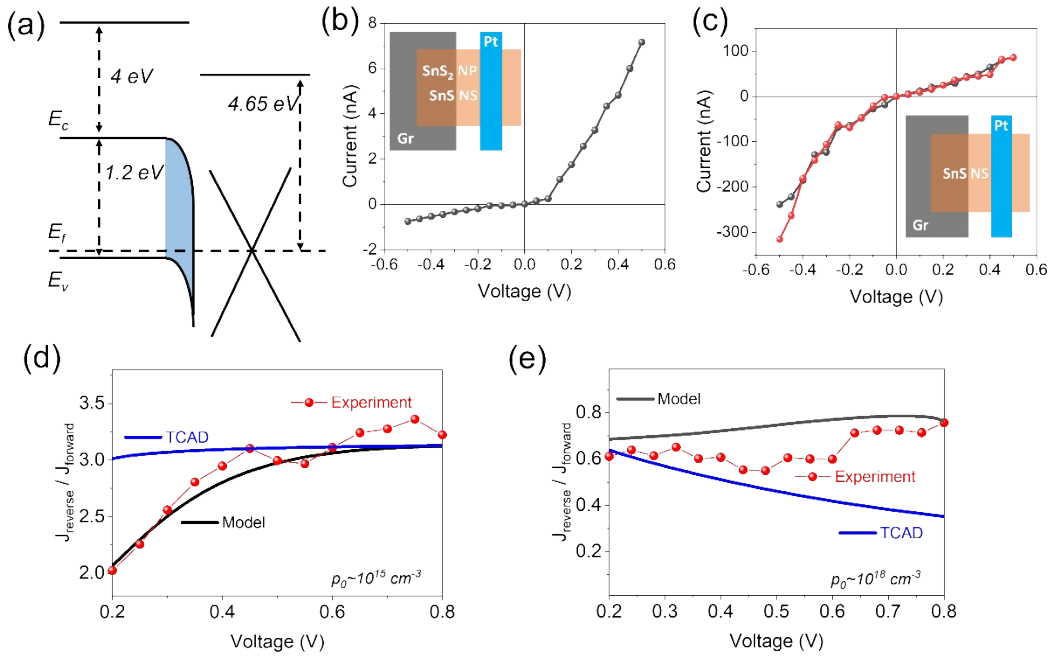


Fig. S10. (a) Energy band diagram of SnS and graphene contact. (b, c) I-V curves of three samples of Gr/NP-NS/Pt and Gr/NS/Pt. (d, e) A comparison of stimulated results from TCAD, calculated results from our model and experimental results for a low (d) and high (e) hole concentration.

To study the transport mechanism at the heterointerface, the bonding-free vdW structure can provide Fermi-pinning free interface. Considering the interdiffusion and defective interface between 2D material and metal prepared by traditional PVD,<sup>22,23</sup> we prefer to use graphene as the electrodes for Fermi-pinning free contact. Parameter for calculation and simulation: The work function of Graphene is 4.65 eV,<sup>24</sup> the electron affinity, bandgap, tunneling effective mass for SnS are 4.0 eV, 1.2 eV and  $0.15m_0$  as shown in Fig. S10a,<sup>4,25,26</sup> the hole concentration of SnS is on the order of  $10^{18} \text{ cm}^{-3}$  and  $10^{15} \text{ cm}^{-3}$  before and after NP decoration.<sup>27</sup> Despite the ultrahigh mobility reported of  $858 \text{ cm}^2 \text{ V}^{-1} \text{ S}^{-1}$ ,<sup>28</sup> the mobility of NS obtained by liquid phase exfoliation usually one/three orders low than that of mechanical exfoliated NS,<sup>29,30</sup> in our calculation, we assume the mobility of SnS is 2 orders lower than that of CVD growth

SnS.<sup>28</sup>

Fig. S10b shows the I-V curves of three samples of Gr/SnS/Pt, which represent a higher reverse current than forward current. Fig. S10d and 10e shows the comparison of stimulated results from TCAD, calculated results from our model and the experimental results for a low (d) and high (e) hole concentration, the good agreement with the variation tendency indicates our model is effective.

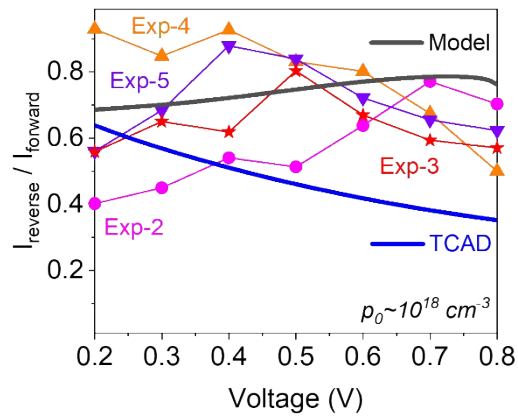


Fig. S11. Comparison of calculated results from TCAD, our model and several experimental results for NS GA-MSM.

Fig. S11 shows the rectification factor of several samples with NS, the difference between theoretical prediction and experimental results may originate from the modulation of mobility by remaining NP, however, all ratios are in the range of [0.3,1].

## Supporting Information Section C: Photoresponse

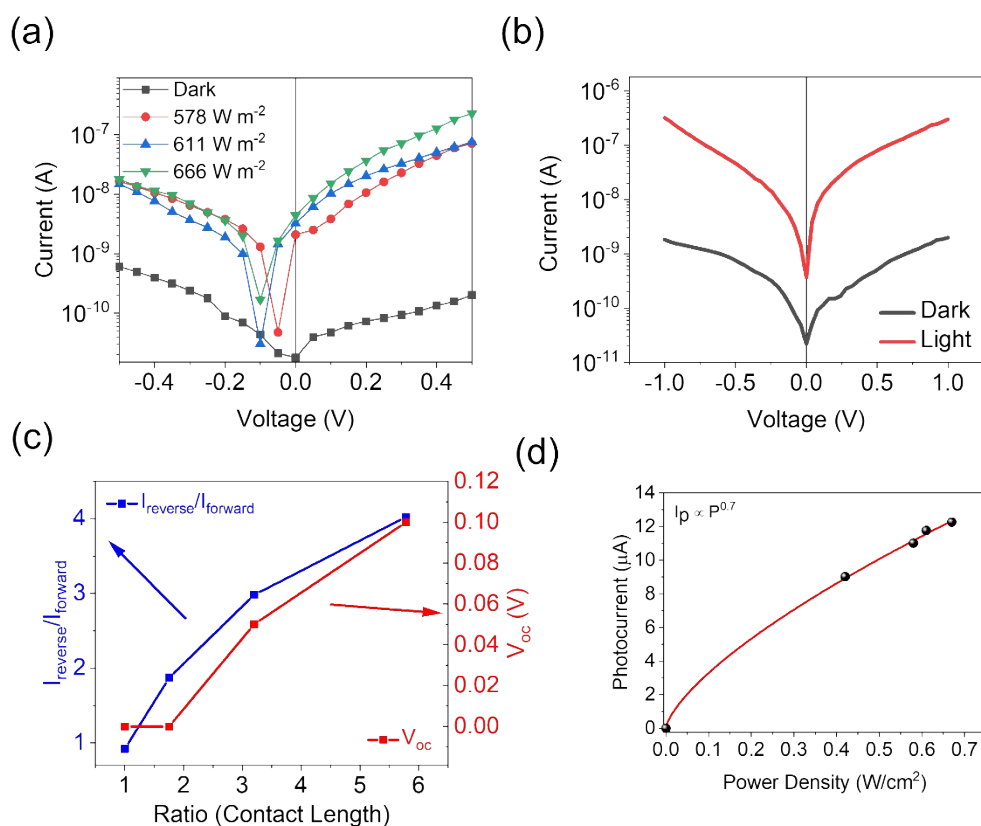


Fig. S12. (a) the I-V curve of NP-NS GA-MSM (Ratio of contact length: 3.2) in the dark and in the light. (b) Current–voltage characteristics of the Gr/NP-NS/Gr with a symmetric contact geometry on a logarithmic scale in the dark and in the light, respectively. (c) The rectification factor ( $I_{reverse}/I_{forward}$ ) and the open-circuit voltage of NP-NS GA-MSM measured at various asymmetric contact geometries in the dark and in the light, respectively. (d) Photocurrent as a function of illumination intensity for the Gr/NP-NS/Gr at a bias voltage of 3 V.

Fig. S12b shows the current–voltage characteristics of the Gr/NP-NS/Gr with a symmetric contact geometry on a logarithmic scale in the dark and in the light, the forward current is almost equal to reverse current without illumination, and no photovoltaic effect can be observed, indicates the rectification and photovoltaic effect originates from the asymmetric contact geometries. Fig. S12c shows the open-circuit

voltage for various samples with different contact ratio.

As the incident light intensity increases, the photocurrent also increases due to more photoexcited carriers are obtained, resulting in a positive relationship between the carrier photogeneration efficiency and the absorption of the incident light. This correlation can be described by a power law :

$$I_p \propto P^\theta \quad (\text{S25})$$

where  $I_p$  is the photocurrent and  $\theta$  reflects the photocurrent efficiency. Curve fitting as shown in Fig. S14, results in a value of  $\theta= 0.7$  for the sunlight stimulator.

The photoresponsivity ( $R$ ) and detectivity ( $D^*$ ) of the  $\text{Sn}_x\text{S}_y$  NP-NS MDvdWHs was calculated based on the following equations:

$$R = I_p/(P \times S) \quad (\text{S26})$$

$$D^* = R/\sqrt{2eI_d/S} \quad (\text{S27})$$

where  $I_p$  is the photocurrent,  $I_d$  is the dark current,  $e$  is elementary charge,  $S$  is the active area under illumination, and  $P$  is the incident light intensity. Without bias voltage, the highest responsivity is estimated as  $9 \times 10^{-4} \text{ A W}^{-1}$  (Fig. 4B). When a bias voltage is applied, the electric field between two graphene electrodes separates more photo-excited electrons and holes in the heterostructure, leading to its higher responsivity. The highest responsivity is estimated as  $35 \text{ A/W}$  at a bias voltage of 3V for NP-NS MDvdWHs, which is several orders of magnitude higher than modern photodetectors based on 2D LPE materials (Table S1).<sup>31,32</sup> Such a high photoresponsivity of the heterostructure can be explained by the high broadband absorption of Gr/ $\text{Sn}_x\text{S}_y$  NP-NS MDvdWHs and the photo gain effect. Electron capture in  $\text{SnS}_2$  NPs leads to an increase in the level of excited NP states and electron tunneling with the formation of a continuous n- $\text{SnS}_2$  layer. The holes are transferred to p-type  $\text{SnS}$  NS and are effectively collected by the graphene electrode before recombination. This leads to high responsivity of NP-NS MDvdWHs, which is one order of magnitude higher than that of NS.<sup>33,34</sup>

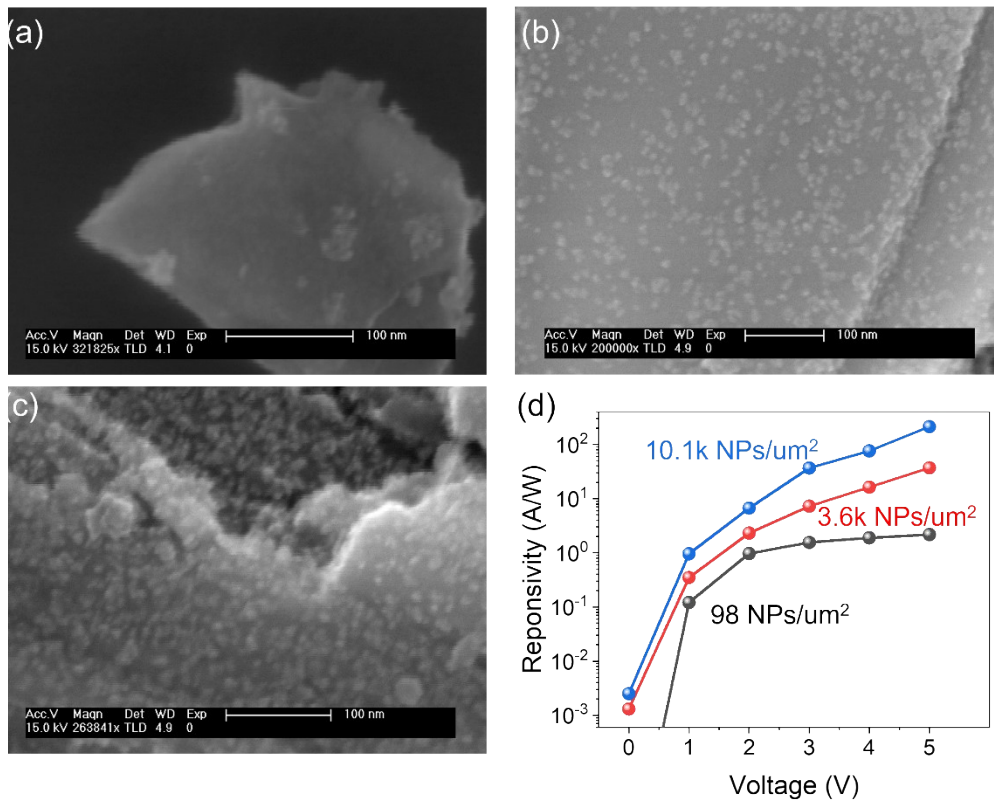


Figure S13. The SEM images of NS (a), NP-NS (b), NP-NS with high concentration of NP (H-NP-NS) (c). (d) Photoresponses of GA-MSM with NS, NP-NS and H-NP-NS measured at various voltage.

We can further increase the concentration of NPs in our device by adding additional NPs solution in NP-NS sample. The SEM image of NS, NP-NS and H-NP-NS are shown in Fig. S13, the concentration of NPs in NS, NP-NS and H-NP-NS are 98 NPs/um<sup>2</sup>, 3600 NPs/um<sup>2</sup> and 10100 NPs/um<sup>2</sup>, respectively. The photoresponse of NS (black), NP-NS (red), H-NP-NS (blue) are shown in Fig. S13d. When the concentration of n-type SnS<sub>2</sub> NPs increases, more electrons will be trapped in NPs, resulting in a trapping lifetime in NPs much longer than the carrier transit time in NS. Considering the gain which given by the ratio of trapping lifetime in NP and carrier transit time in NS, the higher photoresponse can be observed.

Active Layer	Spectral range	Response time [s]	Self-Driven Responsivity [mA W <sup>-1</sup> ]	Responsivity [mA W <sup>-1</sup> ]	Detectivity [cmHz <sup>1/2</sup> W <sup>-1</sup> ]	Ref
SnS/SnS <sub>2</sub>	Simulated sunlight	0.3	$9 \times 10^{-1}$	$3.5 \times 10^4$	$\sim 10^{11}$	This work
TiS <sub>3</sub>	405 nm	8	3.8	3.8	-	35
BP (Black phosphorus)	365~546 nm	0.5	$5.4 \times 10^{-3}$	$2.2 \times 10^{-3}$	-	36
Bi <sub>2</sub> S <sub>3</sub>	365~700 nm	0.1	$8.9 \times 10^{-3}$	$2.1 \times 10^{-1}$	$3.75 \times 10^8$	37
InSe	Simulated sunlight	5	-	$4.8 \times 10^{-3}$	-	38
Te (Tellurium)	350~700 nm and Simulated sunlight	-	-	$1.34 \times 10^{-2}$	$1.7 \times 10^6 \sim 3.1$	32
Bi (Bismuth) NPs	350-700 nm	0.1s	$1.93 \times 10^{-2}$	$2.95 \times 10^{-1}$	-	39
GeSe	350-650 nm	0.2	-	$7.63 \times 10^{-2}$	$1.7 \times 10^{10}$	40
MoS <sub>2</sub>	658 nm	<0.1	-	$\sim 10^{-1}$	-	41
GeP	380nm	0.1s	-	$1.88 \times 10^{-1}$	$2.1 \times 10^{12}$	42
B (Boron)	350~475 nm	0.1~1.5	-	$2.9 \sim 91.7 \times 10^{-3}$ (PEC) $1.7 \sim 2.8 \times 10^{-1}$ (FET)	$\sim 10^8$	43

Table S1. Typical parameters of photodetectors based on layered materials obtained by liquid phase exfoliation.

## References

1. J. R. Brent, D. J. Lewis, T. Lorenz, E. A. Lewis, N. Savjani, S. J. Haigh, G. Seifert, B. Derby and P. O'Brien, *J. Am. Chem. Soc.*, 2015, **137**, 12689-12696.
2. Z. Tian, C. Guo, M. Zhao, R. Li and J. Xue, *ACS Nano*, 2017, **11**, 2219-2226.
3. H. R. Chandrasekhar, R. G. Humphreys, U. Zwick and M. Cardona, *Physical Review B*, 1977, **15**, 2177.
4. M. Patel, H. Kim and J. Kim, *Nanoscale*, 2017, **9**, 15804-15812.
5. M. Patel, A. Chavda, I. Mukhopadhyay, J. Kim and A. Ray, *Nanoscale*, 2016, **8**, 2293-2303.
6. S. Sohila, M. Rajalakshmi, C. Ghosh, A. K. Arora and C. Muthamizhchelvan, *J. Alloy. Compd.*, 2011, **509**, 5843-5847.
7. J. Ahn, M. Lee, H. Heo, J. H. Sung, K. Kim, H. Hwang and M. Jo, *Nano Lett.*, 2015, **15**, 3703-3708.
8. H. Li, B. Zhang, X. Wang, J. Zhang, T. An, Z. Ding, W. Yu and H. Tong, *Frontiers in chemistry*, 2019, **7**, 339.
9. D. H. Youn, S. K. Stauffer, P. Xiao, H. Park, Y. Nam, A. Dolocan, G. Henkelman, A. Heller and C. B. Mullins, *ACS Nano*, 2016, **10**, 10778-10788.
10. X. Fu, P. Ilanchezhian, G. M. Kumar, H. D. Cho, L. Zhang, A. S. Chan, D. J. Lee, G. N. Panin and T. W. Kang, *Nanoscale*, 2017, **9**, 1820-1826.
11. X. L. Wu, J. Y. Fan, T. Qiu, X. Yang, G. G. Siu and P. K. Chu, *Phys. Rev. Lett.*, 2005, **94**, 26102.
12. C. Xin, J. Zheng, Y. Su, S. Li, B. Zhang, Y. Feng and F. Pan, *The Journal of Physical Chemistry C*, 2016, **120**, 22663-22669.
13. L. C. Gomes and A. Carvalho, *Physical Review B*, 2015, **92**, 85406.
14. S. F. Wang, W. Wang, W. K. Fong, Y. Yu and C. Surya, *Sci. Rep.-UK*, 2017, **7**, 39704.
15. J. M. Shannon and K. Nieuwesteeg, *Appl. Phys. Lett.*, 1993, **62**, 1815-1817.
16. M. E. Kiziroglou, X. Li, A. A. Zhukov, P. De Groot and C. H. De Groot, *Solid State Electron.*, 2008, **52**, 1032-1038.
17. S. M. Sze, D. J. Coleman Jr and A. Loya, *Solid State Electron.*, 1971, **14**, 1209-1218.
18. C. R. Crowell and S. M. Sze, *Solid State Electron.*, 1966, **9**, 1035-1048.
19. C. Y. Chang and S. M. Sze, *Solid State Electron.*, 1970, **13**, 727-740.
20. F. A. Padovani and R. Stratton, *Solid State Electron.*, 1966, **9**, 695-707.
21. S. M. Sze, Y. Li and K. K. Ng, *Physics of semiconductor devices*, John Wiley & sons, 2021.
22. Y. Liu, H. Wu, H. Cheng, S. Yang, E. Zhu, Q. He, M. Ding, D. Li, J. Guo, N. O. Weiss, Y. Huang and X. Duan, *Nano Lett.*, 2015, **15**, 3030-3034.
23. Y. Liu, J. Guo, E. Zhu, L. Liao, S. Lee, M. Ding, I. Shakir, V. Gambin, Y. Huang and X. Duan, *Nature*, 2018, **557**, 696-700.
24. J. Zeng and Y. Lin, *Appl. Phys. Lett.*, 2014, **104**, 233103.
25. J. Liang, H. Li, F. Liu and J. Lu, *Advanced Theory and Simulations*, 2021, **4**, 2000290.
26. C. R. Crowell, *Solid State Electron.*, 1969, **12**, 55-59.
27. K. R. Reddy, N. K. Reddy and R. W. Miles, *Sol. Energ. Mat. Sol. C.*, 2006, **90**, 3041-3046.
28. R. Browning, P. Plachinda, P. Padigi, R. Solanki and S. Rouvimov, *Nanoscale*, 2016, **8**, 2143-2148.
29. V. Nicolosi, M. Chhowalla, M. G. Kanatzidis, M. S. Strano and J. N. Coleman, *Science*, 2013, **340**.
30. Z. Lin, Y. Liu, U. Halim, M. Ding, Y. Liu, Y. Wang, C. Jia, P. Chen, X. Duan, C. Wang, F. Song, M. Li, C. Wan, Y. Huang and X. Duan, *Nature*, 2018, **562**, 254-258.
31. C. Xing, X. Chen, W. Huang, Y. Song, J. Li, S. Chen, Y. Zhou, B. Dong, D. Fan and X. Zhu, *ACS*

- Photonics*, 2018, **5**, 5055-5067.
32. Z. Xie, C. Xing, W. Huang, T. Fan, Z. Li, J. Zhao, Y. Xiang, Z. Guo, J. Li and Z. Yang, *Adv. Funct. Mater.*, 2018, **28**, 1705833.
  33. D. Kufer, I. Nikitskiy, T. Lasanta, G. Navickaite, F. H. Koppens and G. Konstantatos, *Adv. Mater.*, 2015, **27**, 176-180.
  34. C. Xie, C. Mak, X. Tao and F. Yan, *Adv. Funct. Mater.*, 2017, **27**, 1603886.
  35. R. Frisenda, E. Giovanelli, P. Mishra, P. Gant, E. Flores, C. Sánchez, J. R. Ares, D. P. de Lara, I. J. Ferrer and E. M. Pérez, *Chem. Commun.*, 2017, **53**, 6164-6167.
  36. X. Ren, Z. Li, Z. Huang, D. Sang, H. Qiao, X. Qi, J. Li, J. Zhong and H. Zhang, *Adv. Funct. Mater.*, 2017, **27**, 1606834.
  37. W. Huang, C. Xing, Y. Wang, Z. Li, L. Wu, D. Ma, X. Dai, Y. Xiang, J. Li and D. Fan, *Nanoscale*, 2018, **10**, 2404-2412.
  38. Z. Li, H. Qiao, Z. Guo, X. Ren, Z. Huang, X. Qi, S. C. Dhanabalan, J. S. Ponraj, D. Zhang and J. Li, *Adv. Funct. Mater.*, 2018, **28**, 1705237.
  39. C. Xing, W. Huang, Z. Xie, J. Zhao, D. Ma, T. Fan, W. Liang, Y. Ge, B. Dong and J. Li, *Acs Photonics*, 2018, **5**, 621-629.
  40. D. Ma, J. Zhao, R. Wang, C. Xing, Z. Li, W. Huang, X. Jiang, Z. Guo, Z. Luo and Y. Li, *ACS Appl. Mater. Inter.*, 2019, **11**, 4278-4287.
  41. C. Chen, H. Qiao, S. Lin, C. Man Luk, Y. Liu, Z. Xu, J. Song, Y. Xue, D. Li and J. Yuan, *Sci. Rep.-UK*, 2015, **5**, 1-9.
  42. C. Li, J. Guo, Y. Zhang, J. Kang, W. Huang, T. Zhai and H. Zhang, *J. Mater. Chem. C*, 2020, **8**, 5547-5553.
  43. D. Ma, R. Wang, J. Zhao, Q. Chen, L. Wu, D. Li, L. Su, X. Jiang, Z. Luo and Y. Ge, *Nanoscale*, 2020, **12**, 5313-5323.